



**HAL**  
open science

## 2D radial-azimuthal particle-in-cell benchmark for $E \times B$ discharges

W Villafana, Federico Petronio, A Denig, M Jimenez, D Eremin, Laurent Garrigues, F Taccogna, Alejandro Alvarez-Laguna, Jean-Pierre Boeuf, Anne Bourdon, et al.

► **To cite this version:**

W Villafana, Federico Petronio, A Denig, M Jimenez, D Eremin, et al.. 2D radial-azimuthal particle-in-cell benchmark for  $E \times B$  discharges. Plasma Sources Science and Technology, 2021, 30 (7), pp.075002. 10.1088/1361-6595/ac0a4a . hal-03285311

**HAL Id: hal-03285311**

**<https://hal.science/hal-03285311>**

Submitted on 13 Jul 2021

**HAL** is a multi-disciplinary open access archive for the deposit and dissemination of scientific research documents, whether they are published or not. The documents may come from teaching and research institutions in France or abroad, or from public or private research centers.

L'archive ouverte pluridisciplinaire **HAL**, est destinée au dépôt et à la diffusion de documents scientifiques de niveau recherche, publiés ou non, émanant des établissements d'enseignement et de recherche français ou étrangers, des laboratoires publics ou privés.

# 2D radial-azimuthal Particle-In-Cell benchmark for $\mathbf{E} \times \mathbf{B}$ discharges

W. Villafana<sup>1,2</sup>, F. Petronio<sup>2,3</sup>, A. C. Denig<sup>4</sup>, M. J. Jimenez<sup>5</sup>, D. Eremin<sup>6</sup>, L. Garrigues<sup>7</sup>, F. Taccogna<sup>8</sup>, A. Alvarez-Laguna<sup>3</sup>, J.P. Boeuf<sup>7</sup>, A. Bourdon<sup>3</sup>, P. Chabert<sup>3</sup>, T. Charoy<sup>3</sup>, B. Cuenot<sup>1</sup>, K. Hara<sup>4</sup>, F. Pechereau<sup>1,3</sup>, A. Smolyakov<sup>5</sup>, D. Sydorenko<sup>9</sup>, A. Tavant<sup>3</sup>, O. Vermorel<sup>1</sup>

<sup>1</sup> CERFACS, 42, avenue Gaspard Coriolis, 31057 Toulouse, France

<sup>2</sup> Safran Aircraft Engines, 27208 Vernon, France

<sup>3</sup> Laboratoire de Physique des Plasmas (LPP), CNRS, Sorbonne Université, École Polytechnique, Institut Polytechnique de Paris, 91120 Palaiseau, France.

<sup>4</sup> Stanford University, Stanford, CA, 94305, United States of America

<sup>5</sup> Department of Physics and Engineering Physics, University of Saskatchewan, 116 Science Place, Saskatoon SK S7N 5E2, Canada

<sup>6</sup> Ruhr University Bochum (RUB), Universitaetsstrasse 150, 44801 Bochum, Germany

<sup>7</sup> LAPLACE, Université de Toulouse, CNRS, F-31062 Toulouse, France

<sup>8</sup> Institute for Plasma Science and Technology (ISTP), CNR, 70126 Bari, Italy

<sup>9</sup> Department of Physics, University of Alberta, Edmonton, Alberta, Canada

E-mail: villafana@cerfacs.fr

13 July 2021

## Abstract.

In this paper we propose a representative simulation test-case of  $\mathbf{E} \times \mathbf{B}$  discharges accounting for plasma wall interactions with the presence of both the Electron Cyclotron Drift Instability (ECDI) and the Modified-Two-Stream-Instability (MTSI). Seven independently developed Particle-In-Cell (PIC) codes have simulated this benchmark case, with the same specified conditions. The characteristics of the different codes and computing times are given. Results show that both instabilities were captured in a similar fashion and good agreement between the different PIC codes is reported as main plasma parameters were closely related within a 5% interval. The number of macroparticles per cell was also varied and statistical convergence was reached. Detailed outputs are given in the supplementary data, to be used by other similar groups in the perspective of code verification.

*Keywords:* benchmark, modified two-stream instability, electron cyclotron drift instability, plasma-wall interactions,  $\mathbf{E} \times \mathbf{B}$  discharges, particle-in-cell

This article may be downloaded for personal use only. Any other use requires prior permission of the author and IOP Publishing. This article appeared in *Plasma Sources Sci. Technol.* **30** 075002 (2021) and may be found at <https://doi.org/10.1088/1361-6595/ac0a4a>

## 1. Introduction

Many devices, such as Hall Effect Thrusters (HET) [1, 2, 3] and magnetron discharges [4, 5] operate in the regime of partially magnetized  $\mathbf{E} \times \mathbf{B}$  plasmas. Though it is generally understood that plasma fluctuations are responsible for the enhanced electron transport, typically larger than what would be expected from the classical collisional theory [6], the exact nature of the instabilities resulting in anomalous electron current is not fully understood. A recent overview of different mechanisms of the instabilities and their interactions can be found in [7].

One such mechanism is the Electron Cyclotron Drift Instability (ECDI) or Electron Drift Instability (EDI) driven by the  $\mathbf{E} \times \mathbf{B}$  electron drift. Over the past decade, this instability has attracted an intense interest as an important source of the anomalous transport in Hall thruster [8, 9, 10, 11, 12]. The instability occurs for the wave propagating in the  $\mathbf{E} \times \mathbf{B}$  direction, perpendicular to the magnetic field. When the wave can also propagate along the magnetic field lines, it may trigger another kind of instability: the Modified Two-Streams Instability (MTSI). Finite value of the electric field perturbation along the magnetic field results in significant electron heating in this direction [13, 14]. Overall, it may result in comparable electron and ion heating [15], but in different directions. The unmagnetized ions are primarily heated up in the  $\mathbf{E} \times \mathbf{B}$  direction, whereas electron heating occurs along  $\mathbf{B}$ . Such anisotropic heating may have important consequences for  $\mathbf{E} \times \mathbf{B}$  discharges. For instance, in the case of magnetically shielded HETs, ion heating might increase the erosion near magnetic poles because of local magnetic field lines parallel to the walls [16]. In a non-magnetically shielded HET, the magnetic field lines are essentially radial at the channel exit and so the electron heating along  $\mathbf{B}$  tends to enhance the flux toward the walls [17]. As a consequence, secondary electron emission (SEE) might increase [18]. Although SEE has a modest impact on electron transport [19], it might lead to other sheath instabilities [20, 21].

The nonlinear coupling of ECDI and MTSI in the presence of plasma-wall interaction poses significant challenges to correctly evaluating the transport properties. The analytical treatment of the kinetic equations provides useful insights but remains difficult to conduct [11, 13]. Thus, it is common to study them numerically with Particle-In-Cell (PIC) simulations. These instabilities are intrinsically multidimensional, so 2D or 3D simulations are required [22]. Unfortunately, most of the time, 3D simulations remain computationally too costly. For instance, only Taccogna *et al.* [23] have captured both the ECDI and the MTSI in 3D PIC simulation using geometrical scaling factors. So, most of the PIC simulations of  $\mathbf{E} \times \mathbf{B}$  discharges are performed in 2D. In particular,

radial azimuthal simulations are appropriate to study the effects of the plasma-wall interaction in HETs. Geometrical effects play a key role in this configuration since the curvature at the walls was found to greatly affect SEE yields, that can be coupled with the ECDI [9]. The setup can be further simplified by neglecting curvature effects while still providing relevant physics insights. By using a Cartesian grid, Croes *et al.* [24] could verify that the ECDI was one important factor explaining electron anomalous transport. Besides, even with no curvature, Tavant *et al.* [21] observed a coupling between the ECDI and SEE. Different regimes of sheath saturation were found possible depending on the choice of the wall material.

In 2D PIC simulations, in addition to the ECDI, the MTSI was identified by Janhunen *et al.* [25] and observed in Petronio *et al.* [26]. Similarly, Hara *et al.* [27] have found the typical radial patterns resembling the MTSI. It was found in [25] that the ECDI and MTSI had the expected two dimensional structure and that both instabilities seemed coupled demonstrating an inverse cascade towards the long wavelengths azimuthally and showing radial structures in the axial current. However, this study was limited to the first microseconds of simulation due to strong electron heating, partially amplified by the absence of the heating saturation mechanism in the simulations. Indeed, in order to capture the appropriate physics, a 2D3V radial-azimuthal simulation setup uses an off-plane axial electric field to maintain a  $\mathbf{E} \times \mathbf{B}$  cross-drift current in the azimuthal direction. Therefore, with periodic boundary conditions in the azimuthal direction, the energy of particles keeps increasing in time due to the imposed axial electric field. This is not the case in a real HET with a finite length between the anode and cathode. One way to circumvent this difficulty and mimic the finite axial length of the discharge is to use a virtual axial length model in the axial/off-plane direction [28, 11]. In this model, the axial displacement of particles is tracked and particles are replaced with cold ones after having traveled the distance corresponding to the effective length of the discharge. The re-injection of particles however has to be handled carefully. For example, Tavant [29] showed that the use of a virtual axial model with random position re-injection effectively results in large numerical instabilities, which can dramatically impact the simulation results. This drawback has already been observed in 1D-azimuthal simulations [10, 30, 31].

Therefore, PIC simulations in the radial-azimuthal plane remain intricate and require a careful analysis of the physics mechanisms of the instabilities as well as a careful treatment of numerical issues. We note here that, in spite of constant progress, the current time and spatial resolution of experimental measurements in  $\mathbf{E} \times \mathbf{B}$  discharges in HET conditions do not allow a detailed validation of the different instabilities observed in simulations [7].

At this stage, the verification of the physics and numerical implementations are important to provide confidence in the numerical results via code benchmarking, i.e. performing a code-to-code comparison. For low temperature plasmas, the 1D discharge benchmark by Turner *et al.* [32] has become a reference for PIC codes, as a way to verify main features such as Monte Carlo algorithms and Poisson solvers. However, this 1D

benchmark case does not capture all the physics of the  $\mathbf{E} \times \mathbf{B}$  discharges, which is more complex due to the presence of the magnetic field and instabilities triggered by the  $\mathbf{E} \times \mathbf{B}$  drift. Recently, a 2D axial-azimuthal benchmark has been carried out by Charoy *et al.* [33] within the framework of the LANDMARK project [34]. In this work, the axial-azimuthal plane of a HET was modeled and seven independent PIC codes successfully reproduced the same ECDI characteristics and representative plasma parameters. In addition to benchmarking the numerical implementations of the independent codes, it also provided information on the existence and effects of the ECDI on the cross-field electron transport.

In the present work, as part of the LANDMARK project, we propose a 2D PIC benchmark for the radial-azimuthal plane of a HET. Our goal is, with a relatively simple configuration, to include both the MTSI and the ECDI physics, compare the predictions of six independent codes, and characterize the nonlinear features of fluctuations and structures arising in simulations. These simulations have been performed by six independent research groups to provide a reference benchmark for the community. In Section 2, the numerical setup is detailed. Then, in Section 3 the discharge behavior is described to study the underlying physics. In Section 4 the results obtained by different codes are compared, and the instabilities characteristics and plasma parameters are verified. Finally, the statistical convergence is discussed.

## 2. Methodology and numerical setup

### 2.1. Numerical setup

For the radial-azimuthal PIC simulations presented in this work, we consider a square 2D Cartesian grid, with square cells, as shown in Figure 1. The azimuthal direction  $y$  is periodic and the curvature is neglected. In a real HET, a dielectric layer would cover the walls in the radial  $z$  direction, but for this benchmark, the simulation domain is instead bounded by two grounded walls with an imposed potential  $\phi_0 = 0$  V. The time step  $\Delta t$  and cell size  $\Delta y = \Delta z$  are chosen to comply to the PIC stability conditions [35],

$$\begin{cases} \Delta y < \frac{\lambda_D}{2}, \\ \Delta t < \frac{0.2}{\omega_{pe}}, \end{cases} \quad (1)$$

where  $\lambda_D = \sqrt{\epsilon_0 k_B T_e / (n_e e^2)}$  is the Debye length and  $\omega_{pe} = \sqrt{n_e e^2 / (m_e \epsilon_0)}$  the plasma frequency. Here,  $\epsilon_0$  is the vacuum permittivity,  $k_B$  the Boltzmann constant,  $n_e$  the electron density,  $e$  the elementary charge and  $m_e$  the electron mass. With  $n_e = n_0 = 5 \times 10^{16} \text{ m}^{-3}$  and  $T_e = T_{e,0} = 10 \text{ eV}$ , we find  $\lambda_D = 100 \mu\text{m}$ ,  $\omega_{pe} = 1.26 \times 10^{10} \text{ rad} \cdot \text{s}^{-1}$  and we set  $\Delta y = 50 \mu\text{m}$  and  $\Delta t = 1.5 \times 10^{-11} \text{ s}$ .

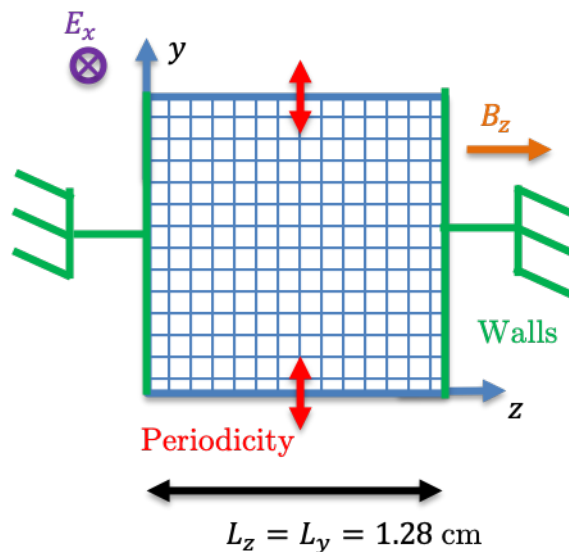


Figure 1: 2D radial-azimuthal ( $z, y$ ) setup.

We consider only electrons and singly charged xenon ions,  $\text{Xe}^+$ , in a collisionless plasma. Collisions were not accounted for in this work because both the ECIDI and MTSI can occur without them [25]. Besides, the collisionless assumption makes the simulations running faster, which is advantageous for benchmarking. Initially, the particles are distributed uniformly in the domain with a density  $n_0 = 5 \times 10^{16} \text{ m}^{-3}$  and a velocity

sampled from a Maxwellian distribution at temperature  $T_{e,0}$  and  $T_{i,0}$ , for electrons and ions, respectively. The simulation is initialized with  $N_{ppc,ini} = 100$  macroparticles per cells (for each species) which gives approximately  $N_{ppc,fin} = 212$  macroparticles per cell at steady-state. We use a constant and uniform radial magnetic field  $B_z$  in the radial  $z$  direction in addition to an off-plane axial electric field  $E_x$  perpendicular to the simulation domain, which produces an  $\mathbf{E} \times \mathbf{B}$  current along the azimuthal  $y$  direction. The particles reaching the walls are removed from the simulation. The electrons are magnetized, while the ions are not. The diagnostic data are averaged during the computation over  $N_a = 1000$  time steps and the output files are generated every  $N_a$ . Numerical and physical parameters are summarized in Table 1.

Table 1: PIC simulations parameters.

Parameters	Symbol	Value	Unit
<b>Simulation domain</b>			
Cell size	$\Delta y = \Delta z$	50	$\mu\text{m}$
Azimuthal length	$L_y$	1.28	cm
Radial length	$L_z$	1.28	cm
Number of cells	$N_{cell}$	$256 \times 256$	
<b>Initial conditions</b>			
Plasma density	$n_0$	$5 \times 10^{16}$	$\text{m}^{-3}$
Ion temperature	$T_{i,0}$	0.5	eV
Electron temperature	$T_{e,0}$	10	eV
Number of particles/cell	$N_{ppc,ini}$	100	
<b>Physical parameters</b>			
Potential at walls	$\phi_0$	0	V
Radial magnetic field	$B_z$	200	G
Axial electric field	$E_x$	10	$\text{kV m}^{-1}$
Virtual axial length	$L_x$	1	cm
<b>Computational parameters</b>			
Time step	$\Delta t$	$1.5 \times 10^{-11}$	s
Average time range	$N_a$	$1000\Delta t$	s
Final time	$t_{max}$	30	$\mu\text{s}$

## 2.2. Virtual axial model

Although we perform a 2D simulation of the radial-azimuthal  $(z, y)$  plane, in order to retrieve the behavior of an HET, a constant electric field  $E_x$  is set in the axial  $x$  direction. Note that the Poisson equation is solved only in the  $(y, z)$  plane at  $x = 0$ . As it is, the modeled system would not reach a steady state due to a constant input of energy, as observed in previous PIC studies [25, 9]. To reach a steady state, a virtual axial model inspired from 1D azimuthal [10, 27, 30] and 2D radial-azimuthal [21, 24, 18] simulations is used and shown in Figure 2.

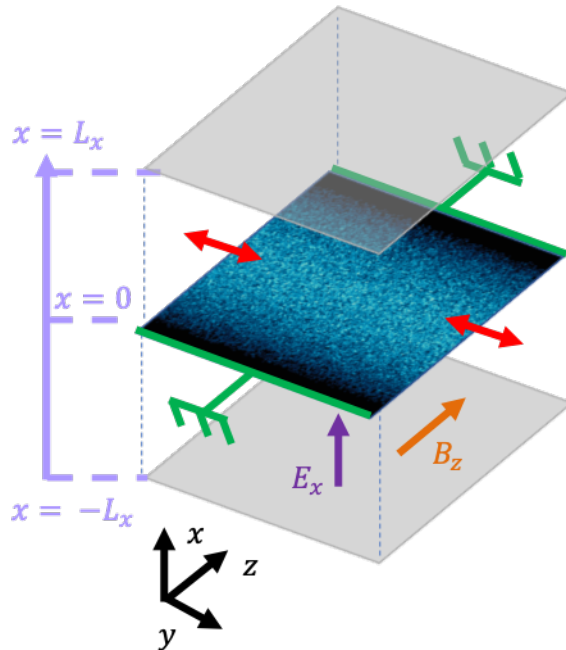


Figure 2: Virtual axial model used for the 2D radial-azimuthal simulation. The plasma dynamics take place in the  $y - z$  plane.

All particles are initialized in the plane located at  $x = 0$ . The  $x$  location of each particle is updated and monitored whether it reaches the virtual axial boundaries situated at  $x = \pm L_x$ . The imposed axial electric field accelerates the ions towards the  $+L_x$  boundary while the magnetized electrons drift in the azimuthal direction. Although electrons tend to be located in the  $x < 0$  space, they gyrate around the magnetic field lines and some may be energetic enough to reach the  $+L_x$  boundary.

Any particle crossing the  $x > |L_x|$  boundaries is reinjected in the plane at  $x = 0$ , with the same  $y$  and  $z$ . The injection velocity is sampled from a Maxwellian distribution at the initial temperatures,  $T_{e,0}$  and  $T_{i,0}$  for electrons and ions, respectively. In this work,  $L_x$  is set to 1 cm. We chose this value to obtain a typical steady state that can take place in a HET. Too small values of  $L_x$  refresh velocities too often, which prevents any relevant physical phenomena to develop as the system is constantly reset to its initial state. Too high values of  $L_x$  can end up in large electron temperatures ( $> 50 - 100$  eV), which is consistent with 1D simulation results [10]. As an example, going from  $L_x = 1$  cm to

$L_x = 2$  cm, increases both the total energy of ions and electrons of  $\sim 15 - 20$  eV at steady state.

### 2.3. Ionization

Particle losses at the walls also need to be compensated to reach a steady state. In this work, we consider a collisionless case generating new particles with a constant source term mimicking ionization, as in previous investigations [36, 33, 12]. Similarly to a real HET, the ionization profile is higher in the center of the channel than at the walls. We have assumed the ionization is uniform in the azimuthal direction and that its radial profile is given by

$$\begin{cases} S(z) = S_0 \cos\left(\pi \frac{z - z_M}{z_2 - z_1}\right) & \text{for } z_1 \leq z \leq z_2, \\ S(z) = 0 & \text{for } z > z_2 \text{ or } z < z_1, \end{cases} \quad (2)$$

with  $S_0$  the maximum value of the source term and  $z_2 - z_1$  the width of the ionization zone. The coordinates  $z_1$  and  $z_2$  are symmetric with respect to  $z_M = L_z/2$ . The width of the ionization zone is chosen to be 1.1 cm ( $\sim 86\%L_z$ ). The maximum of the ionization profile is chosen to be symmetric with respect to the centerline and its width is chosen considering the typical sheaths' dimensions in HET [37]. Using the simulation parameters described above,  $z_1 = 0.09$  cm and  $z_2 = 1.19$  cm. At steady state, the total current exiting at the walls must be equal to the current injected into the system by the ionization term. We can calculate the injected current density  $J_m$  as

$$J_m = e \int_0^{L_z} S(z) dz = \frac{2}{\pi} (z_2 - z_1) e S_0. \quad (3)$$

From Equation 3, we enforce the exiting density current to be  $100 \text{ A} \cdot \text{m}^{-2}$  by setting the maximum value of the source term:  $S_0 = 8.9 \times 10^{22} \text{ m}^{-3} \cdot \text{s}^{-1}$ . For a practical numerical implementation, one should first compute the number  $N_{X_e^+/e^-}$  of physical pairs of  $X_e^+/e^-$  to be injected in the domain at each iteration given by

$$N_{X_e^+/e^-} = L_y \Delta t \int_0^{L_z} S(z) dz. \quad (4)$$

The new particles are injected in the plane  $x = 0$ . The in-plane location  $(y_i, z_i)$  of each  $N_{X_e^+/e^-}$  pair is randomly chosen according to the ionization profile given in Equation 2. Explicitly, we used two random numbers  $\alpha$  and  $\beta$  between 0 and 1, as

$$\begin{cases} y_i = \beta L_y, \\ z_i = \arcsin(2\alpha - 1) \frac{z_2 - z_1}{\pi} + z_M. \end{cases} \quad (5)$$

Finally, the velocity of each particle is sampled from a Maxwellian distribution at  $T_{e,0}$  and  $T_{i,0}$ , for electrons and ions, respectively.

## 3. Results for the reference case with the code by CERFACS

In this section, we present in detail the dynamics of the discharge and of ECDI and MTSI instabilities using the code by CERFACS (detailed in section 4.1.1).

## 3.1. Simulation timeline

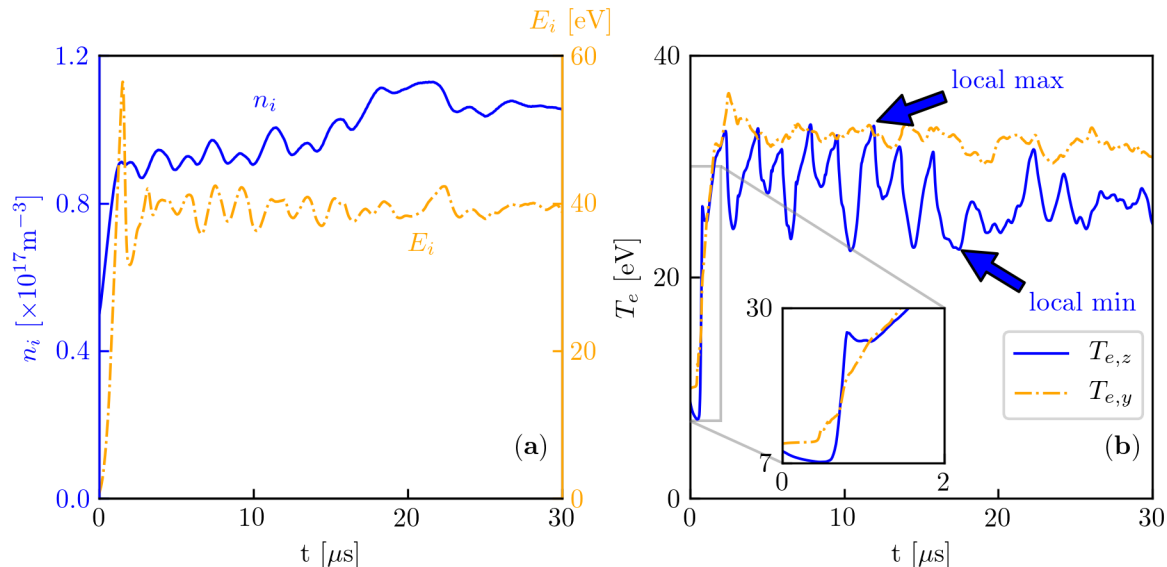


Figure 3: **CERFACS code**: Temporal profiles of ion density  $n_i$  and total ion energy  $E_i$  (a) and radial  $T_{e,z}$  and azimuthal  $T_{e,y}$  electron temperatures (b). In (a), the left y axis in blue corresponds to  $n_i$  and the right one in orange refers to  $E_i$ . Blue arrows in (b) indicate local extrema of  $T_{e,z}$  at  $11.7 \mu\text{s}$  (max) and  $17.5 \mu\text{s}$  (min).

We show in Figure 3 the temporal profiles of ion density  $n_i$ , total ion energy  $E_i$  and electron radial and azimuthal temperatures ( $T_{e,z}$  and  $T_{e,y}$ , respectively). At the beginning of the simulation, for  $\sim 1 \mu\text{s}$ , the ion density increases linearly, because of the imposed ionization source term. Ions gain energy under the effect of the axial electric field for  $\sim 1.5 \mu\text{s}$ . Then, most of the ions have reached the virtual boundary  $L_x = 1 \text{ cm}$ , which brutally dissipates their mean energy. The electron azimuthal temperature  $T_{e,y}$  remains at its initial value for  $0.5 \mu\text{s}$  but then it increases by a factor of 3 between  $0.5 \mu\text{s}$  and  $1.7 \mu\text{s}$ . The radial electron temperature  $T_{e,z}$  first decreases because the most energetic electrons leave the computational domain. Yet, it eventually sharply rises in  $0.2 \mu\text{s}$ . After  $t = 2 \mu\text{s}$ ,  $n_i$ ,  $E_i$ ,  $T_{e,z}$  and  $T_{e,y}$  reach an oscillatory plateau and only at  $t = 17 \mu\text{s}$  the oscillations get damped. This situation results in a radial electron temperature drop and in a small increase of ion density. In contrast,  $E_i$  and  $T_{e,y}$  seem unaffected by the underlying physics and do not experience any clear drop or increase. Finally, after  $t = 20 \mu\text{s}$ , the oscillations seem to be mostly damped and a steady state is reached. These results show that the constant ionization source term successfully compensates particles losses at the walls and that the virtual axial model prevents an accumulation of energy in the system.

In order to understand more precisely the discharge behavior, we focus on specific times of interest. 2D snapshots of relevant parameters are displayed in Figure 4. First, at  $t = 0.53 \mu\text{s}$ , the azimuthal electric field exhibits a purely azimuthal instability

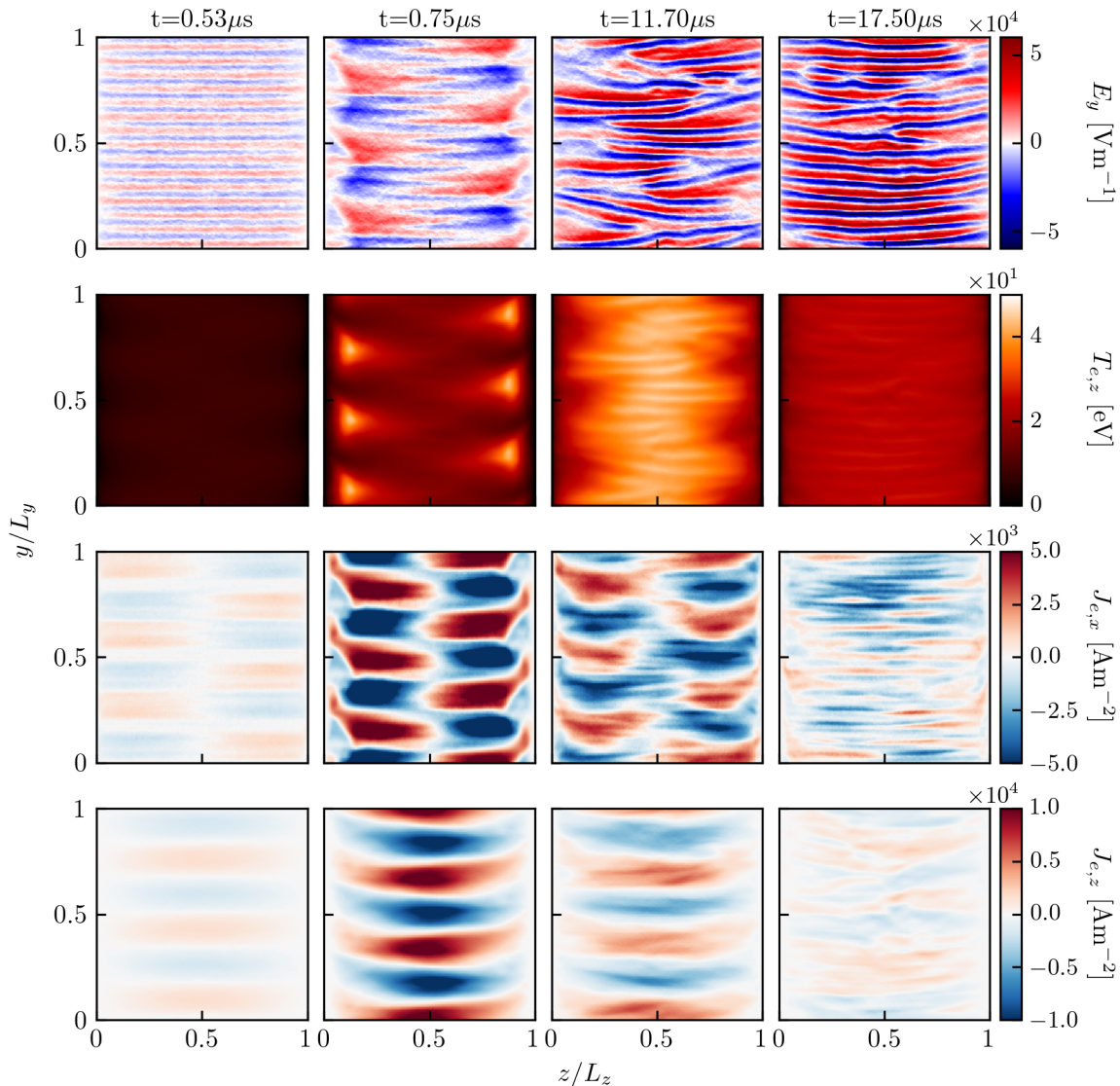


Figure 4: **CERFACS** code: 2D snapshots of azimuthal electric field  $E_y$ , radial electron temperature  $T_{e,z}$ , axial electron current  $J_{e,x}$  and radial electron current  $J_{e,z}$  at times  $t = 0.53 \mu\text{s}$ ,  $t = 0.75 \mu\text{s}$ ,  $t = 11.70 \mu\text{s}$  and  $t = 17.50 \mu\text{s}$ . Local extrema of  $T_{e,z}$  shown in Figure 3 correspond to times  $t = 11.70 \mu\text{s}$  and  $t = 17.50 \mu\text{s}$ .

with a wavelength of the order of 800-900  $\mu\text{m}$ . Another instability, with both radial and azimuthal components has a lower growth rate and develops  $\sim 0.2 \mu\text{s}$  later, as noticeable at  $t = 0.75 \mu\text{s}$ , and also revealed in the axial electron current. Janhunen *et al.* [25] identified these instabilities as the ECDI and the MTSI, respectively. The numerical evidence of two instability mode coexistence and their characteristics will be discussed in detail later. Interestingly, the radial electron current only contains the azimuthal component of the MTSI. The growth of the MTSI actually coincides with the significant increase of the radial electron temperature  $T_{e,z}$  observed in Figure 3. The 2D snapshots show that the electrons first heat up in the near-wall sheath at

periodic locations in the azimuthal direction, which was also clearly observed in [25]. In the present simulation, the azimuthal wavelength is around 4 mm while only a half-wavelength fits in the radial direction with a radial wavenumber  $k_z = \pi/L_z$ . The fast radial electron temperature increase enhances the loss of particles, which explains why the density stops growing linearly, as already noticed in temporal profiles in Figure 3. Moreover, these 2D snapshots can be related to the oscillations observed in the temporal profiles. Indeed, the system oscillates between two distinct states: the first one is seen at  $t = 11.7 \mu\text{s}$  when the MTSI is strong with well defined radial-azimuthal patterns. As a consequence, electrons heat up, which generates a local maximum of the radial electron temperature. Thus, particles leave the domain and the density starts decreasing. The second state is seen at  $t = 17.5 \mu\text{s}$  with a local minimum of the temperature related to a mitigated MTSI. Thus particles tend to fill the domain, leading to a density increase.

### 3.2. Spectral characteristics of the instabilities

In this section, we provide more information on the spectral characteristics of the instabilities described in the previous section which clearly identify them as ECIDI and MTSI. The ECIDI is driven by the overlapping beam mode and cyclotron resonances [38, 39] so the resonant condition in 2D is

$$k_y \approx m \frac{\Omega_{ce}}{v_0}, \text{ with } m = 1, 2, \dots \quad (6)$$

where  $v_0 = E_x/B_z$  is the electron drift velocity in the azimuthal direction and  $\Omega_{ce}$  is the electron cyclotron frequency. Its discrete character as harmonics of the fundamental mode  $k_0 = \Omega_{ce}/v_0$  has been observed in a number of simulations [40, 25, 41]. The MTSI is a long wavelength 2D instability typically with a characteristic wavenumber  $k_y \ll k_0$  [38, 25]. We note also that its growth rate is smaller than that of the ECIDI. Despite its lower growth rate, it becomes very pronounced in simulations at later stages [25].

In the present work, we perform a spectral analysis using the Fast Fourier Transform (FFT) function from the Python package Numpy. In Figure 5, we present a spectral analysis of the results obtained in the previous section. In Figure 5 (a), the 2D FFT on the azimuthal electric field at  $t = 0.4 \mu\text{s}$  shows that the simulation starts with three discrete modes. Two of them have no radial component and only have an azimuthal wavenumber multiple of  $k_0$ . They correspond the first two ECIDI resonances according to Equation 6. The last one has a wavenumber  $k_y \sim 0.2k_0$  below the first ECIDI resonance and a non-zero radial wavenumber. This mode was identified theoretically consistent with MTSI, as described by Janhunen *et al.* [25]. As noted in previous investigations [42, 43], plasma sheath effects make possible the existence of shorter wavenumbers below the geometrical constraint  $k_z = 2\pi/L_z$ . In the present work, the radial wavenumber of the MTSI  $k_z \approx \pi/L_z$  ( $k_z \lambda_D \sim 2.19 \times 10^{-2}$ ) corresponds to a half wavelength between the walls, which agrees with results obtained by Janhunen *et al.* [25].

In Figure 5 (b-c), we show temporal profiles for the MTSI and the first ECIDI resonance. These profiles have been obtained by performing first a 1D FFT in the

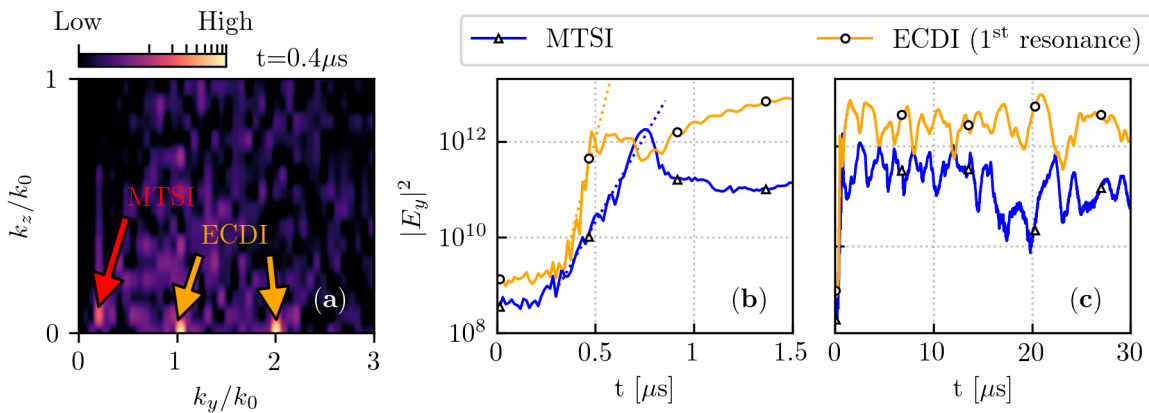


Figure 5: **CERFACS code**: Spectral analysis of the azimuthal electric field  $E_y$ . (a) 2D FFT at linear stage when both ECDI and MTSI start developing. (b) and (c) temporal evolution of the amplitude of the MTSI and ECDI modes in the  $E_y$  spectrum. The amplitude has been integrated over  $k_z$  components. In (b) the dotted lines mark the linear growth of the modes obtained from a least-square method.

azimuthal direction at each radial location, then inferring a mean FFT profile in the azimuthal direction and then finally repeating this process for every output file, distinguishing each FFT coefficient.

From Figure 5 (b), we identify the linear stage for both instabilities, that is  $\sim 0.3$ - $0.73 \mu\text{s}$  for MTSI and  $0.3$ - $0.50 \mu\text{s}$  for the first resonance of ECDI. During this period, the growth is driven by the exponential factor  $\exp(2\gamma t)$  and the growth rate  $\gamma$  can be obtained from a least square method. As noted by Janhunen *et al.* [25], the ECDI has a faster growth rate than the MTSI, except that here, the MTSI does not start growing after the ECDI saturation. In order to get further confidence in the numerical results, we can compare PIC measurements with theoretical results given by the linear dispersion relation  $\omega(\mathbf{k})$ , assuming cold ions [44],

$$1 + k^2 \lambda_D^2 + \frac{\omega - \mathbf{k} \cdot \mathbf{V}_d}{\sqrt{2} k_z \rho \omega_{ce}} e^{-b} \sum_{m=-\infty}^{\infty} Z\left(\frac{\omega - \mathbf{k} \cdot \mathbf{V}_d - m \omega_{ce}}{\sqrt{2} k_z \rho \omega_{ce}}\right) I_m(b) - \frac{k^2 \lambda_D^2 \omega_{pi}^2}{(\omega - k_x v_p)^2} = 0, \quad (7)$$

where  $k_x$ ,  $k_y$ ,  $k_z$  are the components of the wavevector  $\mathbf{k}$ ,  $b = k_{\perp}^2 \rho_e^2$ ,  $k_{\perp}^2 = k_x^2 + k_y^2$ ,  $\rho_e^2 = v_{the}^2 / \omega_{ce}^2$ ,  $v_{the}^2 = k_B T_e / m_e$ ,  $\lambda_D^2 = k_B \epsilon_0 T_e / n_0 q_e^2$ ,  $v_p$  is the ion beam velocity,  $\mathbf{V}_d$  is the electron drift velocity relative to the ions,  $\omega_{ce}$  is the electron cyclotron frequency,  $\omega_{pi}$  is the ion plasma frequency,  $Z(\xi)$  is the plasma dispersion function, and  $I_m(x)$  is the modified Bessel function of the 1st kind. For this 2D case,  $k_x = 0$  and the numerical solution of this relation was achieved through the algorithm developed by Cavalier *et al.* [44] via a fixed point iteration. The theoretical solver was employed using simulation data from  $0.4 \mu\text{s}$ , the time just before the linear growth stage of the instabilities, for which  $n_e = 6.37 \times 10^{16} \text{ m}^{-3}$  and  $T_e = 9.19 \text{ eV}$ . The theoretical growth rates are compared with

PIC measurements in Figure 6.

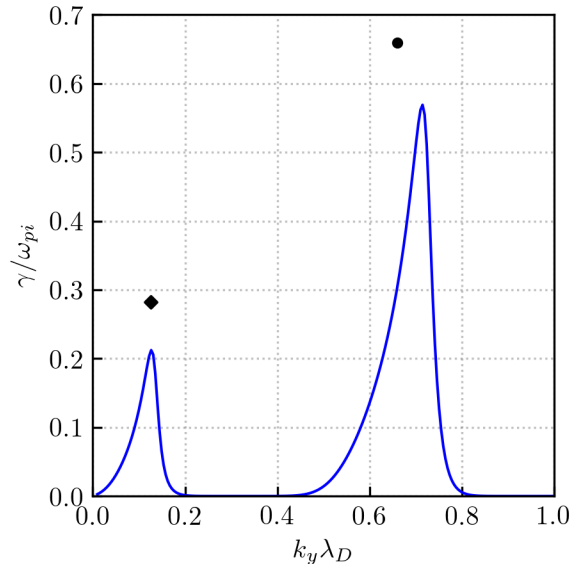


Figure 6: Theoretical growth rates, obtained from Stanford and USASK, using simulation values at the beginning of the linear stage when both ECDI and MTSI start developing for  $k_z \lambda_D = 2.19 \times 10^{-2}$ , set up by the plasma diffusion toward the walls. Symbols represent PIC measurements for MTSI (diamond) and first ECDI resonance (circle) from Figure 5.

From the theoretical dispersion relation, at  $k_z \lambda_D = 2.19 \times 10^{-2}$ , MTSI should feature a resonance at  $k_y \lambda_D = 0.127$ , and ECDI should feature a first resonance at  $k_y \lambda_D = 0.714$ . Overall, both azimuthal wavenumbers and maximum growth rates are in excellent agreement with the instabilities seen in the simulation during the linear stage of growth. This suggests that the initial diffusion toward the radial walls sets up a finite- $k_z$  mode, and the MTSI seen in this study is initiated by this plasma-wall interaction.

At the end of its linear stage, Figure 5 (b) shows that the MTSI is briefly stronger than the ECDI around  $t = 0.75 \mu\text{s}$ , which is coherent with radial-azimuthal patterns appearing in the 2D snapshots at the same time on Figure 4. From Figure 5 (c), it is interesting to notice that the ECDI seems to get weaker when the MTSI strengthens, suggesting that both are coupled. Moreover, we count ten clear peaks in the MTSI FFT temporal profile that precede the same number of radial temperature peaks in Figure 3 (b). Thus, it seems the MTSI drives  $T_{e,z}$ , which is consistent with observations made on the 2D snapshots in the previous section. Between  $t = 15 - 20 \mu\text{s}$ , the MTSI is significantly damped, which coincides with the observed increase of density in Figure 3 (a). At steady state, between  $t = 25 - 30 \mu\text{s}$ , the MTSI stabilizes at a lower level than in the first  $10 \mu\text{s}$  of the simulation. It is not clear why the level is lower and what caused the initial damping in the  $15 - 20 \mu\text{s}$  time range. Necessary investigations will be left for a future work.

## 4. Benchmark results

### 4.1. Code presentations

Seven independent research groups have participated to this benchmark. No code is open source and a detailed description of each of them is provided below.

*4.1.1. CERFACS* The PIC variant of AVIP was used for this work. AVIP [45, 46] is a 3D unstructured-grid plasma solver aimed to handle massively parallel computations. It was developed from AVBP, a well-known fluid solver for reactive gases in industrial geometries [47, 48]. Written in Fortran 90, the code features parallelization with MPI and demonstrates excellent computational performances at high number of processors [49]. For the present simulations, the computational domain consists of square cells sliced into two isosceles right-angled triangles. Therefore the mesh has twice as many cells as the other groups. Displacement of particles is performed by the Haselbacher algorithm [50] and no subcycling is used. Random numbers are generated with the built-in function of Fortran 90 with a hard-coded seed to make runs deterministic. Electrons and ions speeds are respectively updated by the standard Boris and leap-frog schemes. Domain decomposition relies on the external library PARMETIS [51] and it is updated if excessive load unbalance is detected among the processors. The in-plane potential is self-consistently calculated with the Poisson solver MAPHYS developed by INRIA [52, 53] that will soon be available in the PETSc library [54, 55]. MAPHYS returns the potential with an accuracy of the second order and the electric field is computed with a second order accurate Green-Gauss formulation. Double floating point precision is used in the code. AVIP-PIC was verified with the 1D discharge benchmark of Turner *et al.* [32] and the 2D axial-azimuthal benchmark of Charoy *et al.* [33].

*4.1.2. LPP* The 2D3V particle-in-cell code used in the present work is *LPPic*. This Fortran90 code uses a structured Cartesian mesh and is parallelized using MPI domain decomposition. The initial distribution of particles is obtained using a random number generator seed provided by the internal clock of every CPU. All numerical variables are double precision floating points. The Poisson equation is solved using the PFMG solver of the open-source HYPRE [56] library. The potential is obtained with a second order accuracy, while the electric field is calculated from the plasma potential by a centered difference scheme with first order accuracy. The classical leap-frog and Boris schemes are used to move the particles. The code has been verified using the 1D He benchmark by Turner *et al.* [32] and the 2D axial-azimuthal benchmark by Charoy *et al.* [33].

*4.1.3. USASK* The code is a 2D3V PIC based on the explicit leap-frog algorithm. The code uses the Boris scheme to solve particle motion equations. To reduce numerical cost, subcycling of electrons relative to ions is applied [57]. The random number generator is the Maximally Equidistributed implementation [58] of Well Equidistributed Long-period Linear generator WELL19937a [59]. The 2D Poisson's equation in a rectangular

domain periodic in one direction is solved using FFT transformation along the periodical direction, with the FFT procedure based on [60]. The code is written in Fortran 90 and is parallelized with MPI. The particle processing algorithm of the code combines both domain and particle decomposition. The whole simulation domain is split into subdomains of the same size, the number of the subdomains is several times smaller than the total number of MPI processes. Particles belonging to the same subdomain may be shared between several processes. The balance of particle load between all MPI processes is achieved by changing the numbers of processes advancing particles in the subdomains. Double floating-point precision is used for all calculations in the code.

*4.1.4. Stanford* The PIC code is written in C++ using MPI as the means of parallelization. Particle decomposition is used to split the number of macroparticles as evenly as possible between the different processors. Domain decomposition is used by the Poisson solver, HYPRE [56], with a symmetric SMG method as the preconditioner and a GMRES solver. A structured, rectangular grid is used. Double precision is used for all numerical variables. Random numbers are generated using the C Standard General Utilities Library by initializing different seed values for each individual processor. This benchmarking effort motivated the implementation of code acceleration techniques to speed up data management. This code has been benchmarked with other codes through the 2D axial-azimuthal benchmark by Charoy *et al.* [33] and tested for other instability cases [36, 61]

*4.1.5. ISTP* The 2D PIC code [18] developed at ISTP is a combination of previous 1D-radial [62, 63, 64] and 1D-azimuthal [30] PIC codes. The code is written in Fortran90 and it uses a structured, uniform, rectangular grid. The version used for the present benchmark is serial and performances reported in Table 2 refer to double precision option. The long period ( $> 2 \times 10^{18}$ ) random number generator RAN2 of Numerical Recipes [60] is implemented. Linear functions are used to interpolate particles onto the grid and the Poisson equation is solved by the cyclic reduction algorithm implemented in the routine PWSCRT of the open-source FISHPACK90 library [65]. The leap-frog with Buneman-Boris scheme is used as solver of particle equation of motion.

*4.1.6. RUB* The PIC code used in the present benchmark differs from our group's implicit energy-conserving code utilized in the axial-azimuthal benchmark [33]. It was now based on the standard explicit leapfrog time integration scheme. By employing the same approach as for the other codes but a different parallelization means, the intention was to demonstrate the latter's benefits. Except for the field solver, the code was parallelized on a graphics processing unit using the CUDA extension of the C programming language and a two-dimensional analog of the fine-sorting algorithm described in [66]. The field solver was implemented on a CPU using a combination of the FFT algorithm in the azimuthal direction and a tridiagonal solver in the radial direction for each of the azimuthal harmonics. The latter was based on the Thomas algorithm.

Only one thread on CPU was utilized for the field solver. Such an implementation was balanced as the CPU and the GPU parts demonstrated comparable execution time for the typical parameters. The long-period xorshift128 algorithm proposed in [67] has been used as a random number generator, with each thread starting initially with a randomly chosen seed.

*4.1.7. LAPLACE* The 2D3V particle-in-cell code used in the present work is written in Fortran90 and uses a structured Cartesian mesh. To exploit the modern architecture of processors, a hybrid technique that combines distributed memory (MPI libraries) between cores and shared memory with Open Multi-Processing (OpenMP) between threads is considered [68, 12]. A particle decomposition is employed, the initial particles being equally distributed between MPI cores and OpenMP threads. To reduce computational time during array accessibility due to random positions of particles with respect to the meshes of the simulation domain, a sorting algorithm has been implemented [69]. The Poisson's equation is solved with the parallel sparse direct linear solver (PARDISO) subroutine included in the Intel®Math kernel Library (Intel®MKL) [70]. The classical leap-frog and Boris schemes are used to move the particles. The code has been verified using the 2D axial-azimuthal benchmark by Charoy *et al.* [33].

#### *4.2. Code comparisons*

The six groups have simulated the test-case presented in Section 3. In Table 2, this reference case is referred as Case A. Four groups have also simulated two supplementary cases with a higher initial number of particles per cell ( $N_{ppc,ini} = 200$  or  $400$ , which correspond respectively to Case B and Case C) to study the statistical convergence which will be analyzed in details in Section 4.5. The main code characteristics are also given in Table 2, along with the corresponding simulation times.

The average computing times show that results for all codes were rather obtained quickly, which is greatly beneficial for benchmarking. Moreover, the comparison of elapsed times on the cases A, B and C highlights the importance of parallel scalability for each particular code. For this particular benchmark, using a particle decomposition along with GPU seems especially effective. The presented runtimes cannot be directly compared between codes as each team used different machines and compilers; besides, GPU and purely CPU based codes remain difficult to compare in terms of computing performances. Yet, the present diversity of the codes provides a reference point for other codes similar to one used in the benchmark.

#### *4.3. Comparison of main plasma parameters*

First, we study the reference case (case A) simulated by all the groups. We see in Figure 7 (a-c) that all temporal profiles of density and radial electron temperature are in very good agreement during the first  $3 \mu\text{s}$ . The linear increase of density displays the same slope while the sharp rise of radial electron temperature occurs around the same

Table 2: Code characteristics. Explicit pusher refers to the standard Leap-frog/Boris algorithm.  $\star$  and  $\star\star$  symbols respectively refer to the particles (speed, position and weight) and to the fields (potential and electric field).

	CERFACS	LPP	USASK	Stanford	ISTP	RUB	LAPLACE
<b>Code implementation</b>							
Language	Fortran	Fortran	Fortran	C++	Fortran	CUDA C + C	Fortran
Parallelization	MPI	MPI	MPI	MPI	No	CUDA	MPI/OpenMP
Decomposition	Domain	Domain	Domain	Particle	No	Particle	Particle
Grid type	Unstructured	Structured	Structured	Structured	Structured	Structured	Structured
CPU/GPU type	Intel Skylake	Intel Haswell	Intel Skylake	Intel Sandy Bridge	Intel Ivy-Bridge	NVIDIA Volta (GPU) + Intel Skylake (CPU)	Intel Skylake
	2x18 cores/node @ 2.3GHz - 96 GB	2x12 cores/node @ 2.6GHz - 64 GB	2x20 cores/node @ 2.4GHz - 202 GB	32 cores/node @ 2.6GHz - 32 GB	2x12 cores/node @ 2.4GHz - 256 GB	5120 cores (GPU) + 10 cores (CPU) @ 1.5GHz - 32 GB (GPU) + @ 2.2GHz - 96 GB (CPU)	2 x 18 cores/node @ 2.30GHz - 64 GB
<b>Code module</b>							
Pusher	Explicit	Explicit	Explicit	Explicit	Explicit	Explicit	Explicit
Poisson solver	MAPHYS	HYPRE	FFT	HYPRE	Fishpack	FFT+Thomas	PARDISO
Order of accuracy							
Potential	2	2	2	2	2	2	2
Electric field	2	1	2	2	1	1	1
Floating-point precision	Double	Double	Double	Double	Double	Single* Double**	Single* Double**
<b>Simulation time for 30 <math>\mu</math>s (elapsed time)</b>							
Case A	35 h	64 h	51 h	168 h	306 h	11 h	12 h
$N_{ppc,fin} \approx 212$	(288 CPU)	(144 CPU)	(256 CPU)	(64 CPU)	(1 CPU)	(1 GPU + 1 CPU)	(180 CPU)
Case B	50 h	205 h	98 h	NA	NA	14 h	17 h
$N_{ppc,fin} \approx 424$	(540-900 CPU)	(72 CPU)	(256 CPU)			(1 GPU + 1 CPU)	(180 CPU)
Case C	77 h	152 h	122 h	NA	NA	29 h	27 h
$N_{ppc,fin} \approx 848$	(540-900 CPU)	(216 CPU)	(256 CPU)			(1 GPU + 1 CPU)	(180 CPU)

instant and experiences a similar growth. Therefore, all groups seem to describe the same discharge dynamics at early times, including the MTSI onset and growth.

After the first 3  $\mu$ s, we see in Figure 7 (b-d) that the electron density and temperature exhibit a complex oscillatory behavior and discrepancies between the results of the different codes are observed. One of the major factors explaining these discrepancies is the use of different Random Number Generators (RNG) at initialization. Indeed, in a supplementary test (not presented here) each group tried to use the same initial locations for macroparticles to mitigate the effect of RNG. The obtained transients for both temperature and density were then extremely close and discrepancies were within statistical uncertainties. For  $t > 20 \mu$ s, Figure 7 (b-d) shows that both temperature and density reach an oscillatory quasi-steady-state.

In order to compare more precisely the results, the ion density and electron temperature are averaged both azimuthally and in time. These radial profiles are shown in Figure 8. The time interval for averaging is set to be 25-30  $\mu$ s to average over several small oscillations. Both ion density and total electron temperature profiles exhibit an excellent agreement between all codes. The most significant differences appear in the centerline but they remain in a  $\pm 2.5\%$  interval around the mean profile. Thus, in spite of the oscillations observed on Figure 7 (b-d), we show here that similar plasma parameters are obtained for all the codes using different RNG.

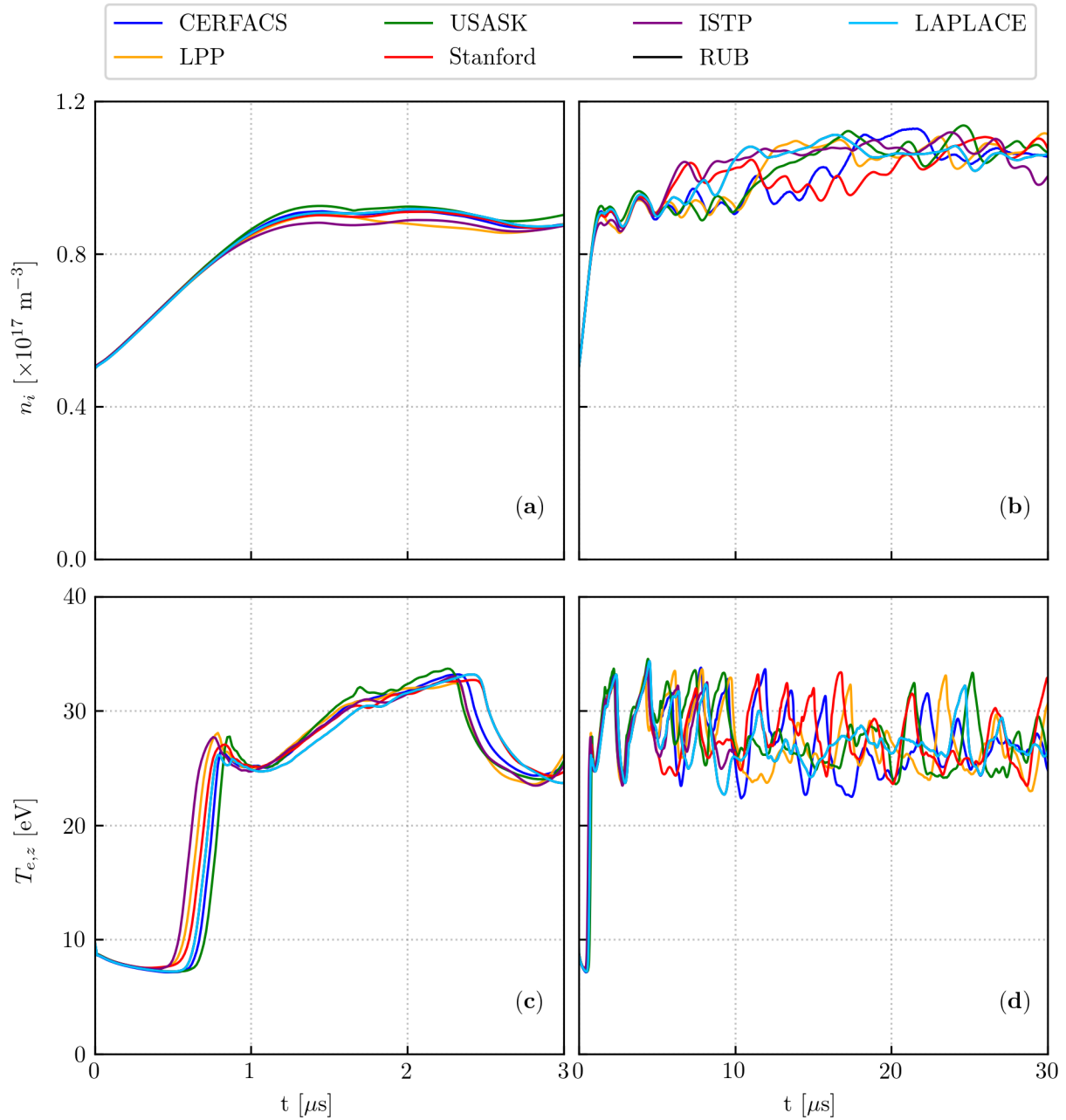


Figure 7: **Case A:** Temporal profiles of plasma density (a) up to 3  $\mu\text{s}$  and (b) for the whole simulation time. (c) and (d) Temporal profiles of radial electron temperature on the same time ranges.

#### 4.4. ECDI-MTSI coupling

We have seen in Section 3.2 that the observed oscillations are related to a coupling between ECDI and MTSI. The presence of both instabilities for all the codes is confirmed in Figure 9, with 1D FFT performed in the azimuthal direction. The azimuthal component of the MTSI is retrieved with a wavenumber  $k_y \approx 0.07k_0$ , while we observe

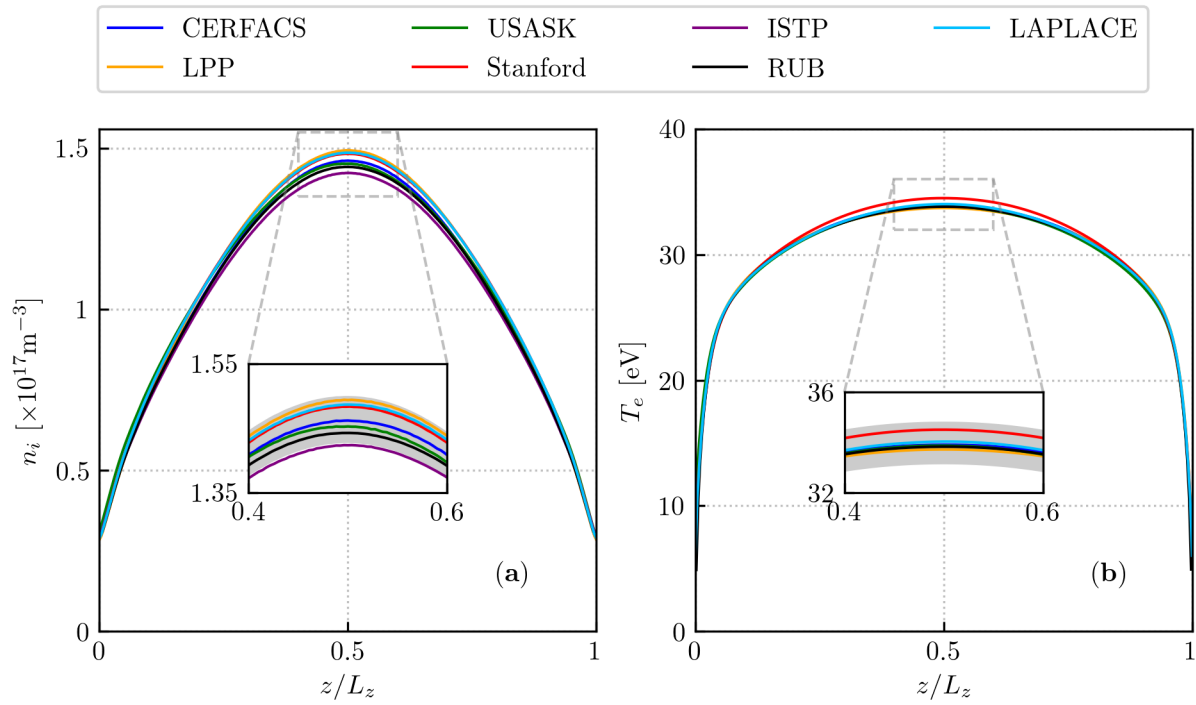


Figure 8: Mean radial profiles of ion density (a) and total electron temperature (b), averaged over 25-30  $\mu\text{s}$ . A zoom on the centerline highlights the discrepancies between the codes. On (b) several profiles are superimposed. The shaded gray area indicates the range  $\pm 2.5\%$  around the averaged radial profiles of all the groups.

the first two ECDI resonances at  $k_y \approx k_0$  and  $k_y \approx 2k_0$ .

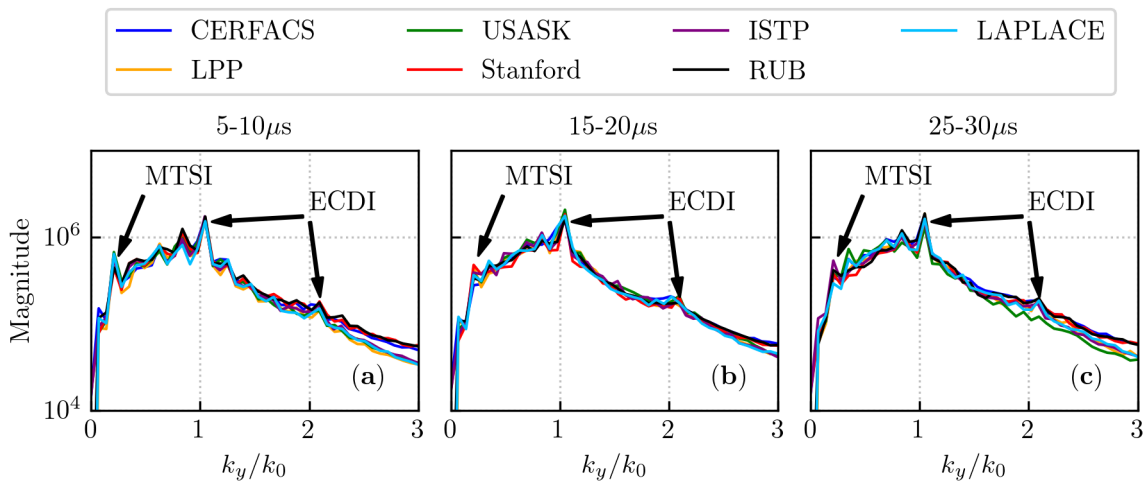


Figure 9: 1D azimuthal FFT of the azimuthal electric field  $E_y$ , averaged over all radial positions and over three temporal intervals: (a) 5-10  $\mu\text{s}$ , (b) 15-20  $\mu\text{s}$ , (c) 25-30  $\mu\text{s}$ . MTSI and ECDI resonances are indicated by arrows.

Although both the ECDI and the MTSI appear distinctly, Figure 9(a) points out that the MTSI is more important at the beginning of the simulation (between 5-10  $\mu\text{s}$ ) and then becomes weaker with time, which echoes with the previous observation on temporal profiles in Section 4.3: at some point, the radial electron temperature is decreasing for all codes, which leads to a density increase. Besides, we can notice some intermediate peaks between the MTSI wavenumber and the first ECDI resonance, especially at the beginning of the simulation. Their nature was not clearly identified and is left for further work. Finally, after the first ECDI resonance, the k-spectra decrease exponentially. The second resonance is still observable with a much lower amplitude and is surrounded by what seems to be numerical noise. At high frequencies, LPP, ISTP, LAPLACE and USASK seem to have lower noise levels that might be related to the use of different Poisson solvers and subsequent implementations.

Overall, we have found that the 1D FFT profiles are also very similar in the different codes, throughout the whole simulation.

#### 4.5. Statistical convergence

In PIC simulations, the use of macroparticles can generate numerical noise. Okuda and Birdsall [71] have shown that this noise can be viewed as numerical collisions with a frequency given by

$$\nu_{num} = \frac{\pi\omega_{p,e}}{16N_{De}}, \quad (8)$$

with  $N_{De}$  the number of macroparticles in a Debye sphere. These numerical collisions can have a significant impact on the discharge behavior, which may lead to misinterpretation of the simulation results. At steady state, the Debye length is around 125  $\mu\text{m}$  in most of the domain. For the reference Case A, the mean number of numerical particles per squared cell at steady state being 212, we can roughly estimate the ratio  $\nu_{num}/\omega_{p,e} \approx 4.72 \times 10^{-5}$ . According to [72], this ratio must be below  $10^{-4}$  to ensure negligible numerical collisions, which is the case here for all groups.

However, to further confirm that numerical collisions are truly negligible and that statistical convergence is reached, tests with different numbers of particles per cell have been performed by five groups. The initial number of macroparticles  $N_{ppc,ini}$  per cell was varied from 6, 12, 25, 50, 100, 200, 400 up to 800 particles. Then, the mean density at steady state was computed by taking the averaged density between 25 and 30  $\mu\text{s}$  and shown in Figure 10 (a) depending on the final number of particles per cell.

We see that when a too low number of macroparticles per cell is used, the density can increase by more than 10% if  $N_{ppc,fin}$  is multiplied by two, which means that the statistical convergence has not been reached. From 100-200 macroparticles per cell, the mean ion density becomes much less sensitive to  $N_{ppc,fin}$  and a plateau at approximately  $n_i \approx 2.17n_0$  is reached. The curves fluctuate around this value because of the natural variability around the mean ion density. In Figure 10 (b), radial profiles of the ion density is displayed for the CERFACS's code and we can see that convergence also appears for a number of macroparticles around  $N_{ppc,fin} = 100-200$ . We note that the

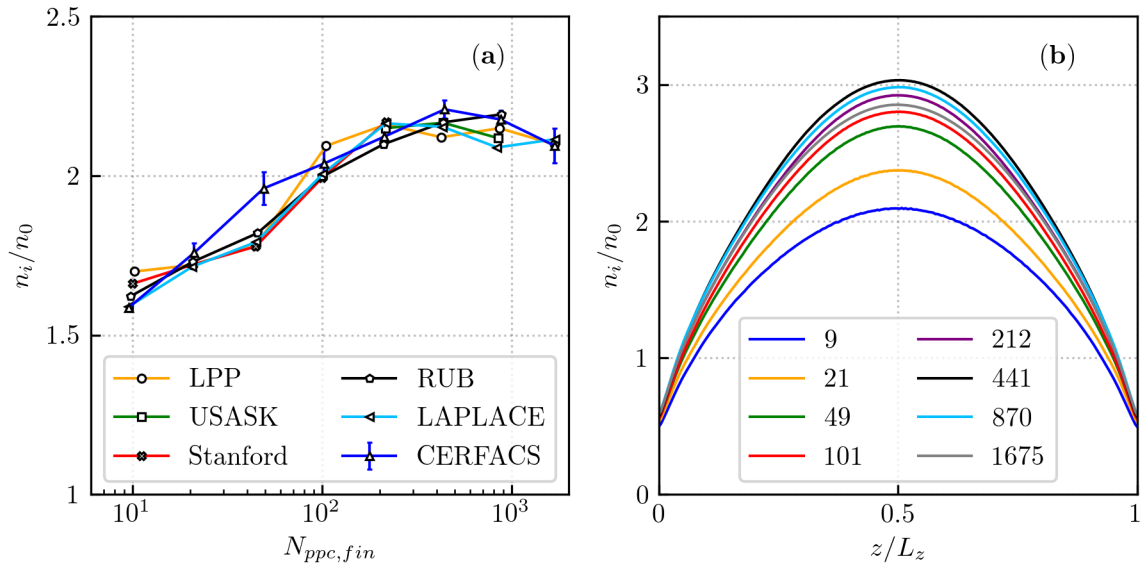


Figure 10: Assessment of statistical convergence between 25-30  $\mu\text{s}$ : (a) mean value of ion density for five groups and (b) averaged radial profiles of density for CERFACS's code for various final number of macroparticles per square cells. In (a) error bars for CERFACS indicate the standard deviation around the mean value. The baseline case has around 212 particles per squared cell at steady state. In (b) radial profiles converge from light/green colors towards dark/blue colors.

reference case presented in the previous sections is well converged with more than 200 macroparticles per cell. The criteria of 100-200 particles per cell to reach statistical convergence agrees with previous conclusions from Charoy *et al.* [33].

## 5. Conclusion and prospective

In this paper, a 2D radial-azimuthal benchmark for  $\mathbf{E} \times \mathbf{B}$  discharges was presented. For this benchmark, collisionless 2D3V-PIC models were used with a virtual axial reinjection model and a fixed ionization source term. The virtual axial model limits the energy growth by removing the high energy tail of the energy distribution functions. Besides, particle losses at the walls are compensated by imposing an ionization source term, similarly to Refs. [33, 12]. These two features provide a framework for benchmarking by allowing the discharge to reach a steady-state. Despite its apparent simplicity, this test-case was chosen as it captures two important instabilities: the ECDI and the MTSI. Both exhibit characteristics that are in agreement with the linear theory and, moreover, they are found to be coupled, which was also noticed by Janhunen *et al.* [25].

Six independent PIC codes have simulated the same test-case. In spite of their differences, all the codes retrieved the ECDI and the MTSI at wavenumbers predicted by the theory. They also converged within a 5% interval on relevant plasma parameters.

Transients are important in this configuration because they directly give an assessment of the ECDI and the MTSI growth and coupling. From temporal profiles and 1D FFTs, all the codes captured a similar development and interaction between both instabilities. Because of the use of different RNG, the transients can be shifted but the main steps of the simulation were eventually retrieved. Finally, the statistical convergence of the results was assessed. It appeared that at least 100-200 macroparticles per cell are needed. A similar conclusion was found in [33] and this criteria could be used for future 2D PIC simulations.

The main goal of this work was to provide confidence on radial-azimuthal simulations, in which the results can be difficult to analyze due to the coupling between ECDI and MTSI or the use of artificial models to deal with the axial direction. Thanks to the benchmark presented in this paper, every radial-azimuthal code can be verified, which paves the way to further investigations accounting for wall and sheath effects. Moreover, even if we made some simplifying assumptions, such as neglecting the presence of neutrals or not accounting for self-consistent ionization, this case can also be used for insightful parametric studies. For instance, by varying the ionization source term, we can define the plasma density at steady-state, a parameter which plays a role in the instability dispersion relations. Hence, the role of this parameter on the ECDI or MTSI onset could be more easily studied.

## Acknowledgments

W. Villafana and F. Petronio acknowledge financial support from a Safran Aircraft Engines doctoral research award as well as from the Association Nationale de la Recherche et de la Technologie (ANRT) as part of a CIFRE convention. The work at LPP and CERFACS has been partially funded by ANR (n° ANR-16-CHIN-003-01) and Safran Aircraft Engines within the project POSEIDON. The work at LPP was granted access to the HPC resources of CINES under the allocations A0060510439 and A0080510439 made by GENCI. The work at CERFACS was performed using HPC resources from GENCI- [CINES/IDRIS/TGCC] (Grant 2020 - [A0032B10157]). Work of A. Smolyakov, M. Jimenez, and D. Sydorenko was supported by the U.S. Air Force Office of Scientific Research FA9550-18-1-0132 and FA9550-21-1-0031, NSERC Canada, and by computational facilities of Compute Canada. F. Taccogna gratefully acknowledges financial support of Italian minister of university and research (MIUR) under the project PON "CLOSE to the Earth" ARS ARS01-00141. D. Eremin gratefully acknowledges support by DFG (German Research Foundation) within the project framework SFB-TR 87. K. Hara and A. Denig appreciate the support by the Air Force Office of Scientific Research under Award No. FA9550-18- 1-0090 and by the US Department of Energy, Office of Science, Office of Fusion Energy Sciences, under Award No. DE-SC0020623. The work at Stanford was performed using resources from the Stanford HPC Center. The work at Laplace was performed using HPC resources from CALMIP (Grant 2013-P1125).

## References

- [1] D. Goebel and I. Katz, *Fundamentals of Electric Propulsion: Ion and Hall Thrusters*. JPL Space Science and Technology Series, Wiley, 2008.
- [2] A. N. Smirnov, Y. Raitses, and N. J. Fisch, “Electron cross-field transport in a miniaturized cylindrical Hall thruster,” *IEEE Transactions on Plasma Science*, vol. 34, no. 2, pp. 132–141, 2006.
- [3] C. Boniface, L. Garrigues, G. J. M. Hagelaar, J. P. Boeuf, D. Gawron, and S. Mazouffre, “Anomalous cross field electron transport in a Hall effect thruster,” *Applied Physics Letters*, vol. 89, no. 16, p. 161503, 2006.
- [4] S. Tsikata and T. Minea, “Modulated electron cyclotron drift instability in a high-power pulsed magnetron discharge,” *Phys. Rev. Lett.*, vol. 114, p. 185001, May 2015.
- [5] J.-P. Boeuf and B. Chaudhury, “Rotating instability in low-temperature magnetized plasmas,” *Phys. Rev. Lett.*, vol. 111, p. 155005, Oct 2013.
- [6] N. Meezan, W. Hargus, and M. Cappelli, “Anomalous electron mobility in a coaxial Hall discharge plasma,” *Physical review. E, Statistical, nonlinear, and soft matter physics*, vol. 63, p. 026410, 03 2001.
- [7] I. D. Kaganovich, A. Smolyakov, Y. Raitses, E. Ahedo, I. G. Mikellides, B. Jorns, F. Taccogna, R. Gueroult, S. Tsikata, A. Bourdon, J.-P. Boeuf, M. Keidar, A. T. Powis, M. Merino, M. Cappelli, K. Hara, J. A. Carlsson, N. J. Fisch, P. Chabert, I. Schweigert, T. Lafleur, K. Matyash, A. V. Khrabrov, R. W. Boswell, and A. Fruchtman, “Physics of ExB discharges relevant to plasma propulsion and similar technologies,” *Physics of Plasmas*, vol. 27, no. 12, p. 120601, 2020.
- [8] J. C. Adam, A. Heron, and G. Laval, “Study of stationary plasma thrusters using two-dimensional fully kinetic simulations,” *Physics of Plasmas*, vol. 11, no. 1, pp. 295–305, 2004.
- [9] A. Héron and J. C. Adam, “Anomalous conductivity in Hall thrusters: Effects of the non-linear coupling of the electron-cyclotron drift instability with secondary electron emission of the walls,” *Physics of Plasmas*, vol. 20, no. 8, p. 082313, 2013.
- [10] T. Lafleur, S. D. Baalrud, and P. Chabert, “Theory for the anomalous electron transport in Hall effect thrusters. i. insights from particle-in-cell simulations,” *Physics of Plasmas*, vol. 23, no. 5, p. 053502, 2016.
- [11] T. Lafleur, S. D. Baalrud, and P. Chabert, “Theory for the anomalous electron transport in Hall effect thrusters. ii. kinetic model,” *Physics of Plasmas*, vol. 23, no. 5, p. 053503, 2016.
- [12] J. P. Boeuf and L. Garrigues, “ExB electron drift instability in Hall thrusters: Particle-in-cell simulations vs. theory,” *Physics of Plasmas*, vol. 25, no. 6, p. 061204, 2018.
- [13] N. A. Krall and P. C. Liewer, “Low-frequency instabilities in magnetic pulses,” *Phys. Rev. A*, vol. 4, pp. 2094–2103, Nov 1971.
- [14] D. E. Hastings and E. Niewood, “Theory of the modified two stream instability in an mpd thruster,” 1 1989.
- [15] J. B. McBride, E. Ott, J. P. Boris, and J. H. Orens, “Theory and simulation of turbulent heating by the modified two-stream instability,” *The Physics of Fluids*, vol. 15, no. 12, pp. 2367–2383, 1972.
- [16] I. G. Mikellides and A. L. Ortega, “Growth of the modified two-stream instability in the plume of a magnetically shielded Hall thruster,” *Physics of Plasmas*, vol. 27, no. 10, p. 100701, 2020.
- [17] M. Sengupta and A. Smolyakov, “Mode transitions in nonlinear evolution of the electron drift instability in a 2d annular ExB system,” *Physics of Plasmas*, vol. 27, no. 2, p. 022309, 2020.
- [18] F. Taccogna, P. Minelli, Z. Asadi, and G. Bogopolsky, “Numerical studies of the ExB electron drift instability in Hall thrusters,” *Plasma Sources Science and Technology*, vol. 28, p. 064002, jun 2019.
- [19] L. Garrigues, G. J. M. Hagelaar, C. Boniface, and J. P. Boeuf, “Anomalous conductivity and secondary electron emission in Hall effect thrusters,” *Journal of Applied Physics*, vol. 100, no. 12,

- p. 123301, 2006.
- [20] D. Sydorenko, A. Smolyakov, I. Kaganovich, and Y. Raitses, “Plasma-sheath instability in Hall thrusters due to periodic modulation of the energy of secondary electrons in cyclotron motion,” *Physics of Plasmas*, vol. 15, no. 5, p. 053506, 2008.
  - [21] A. Tavant, V. Croes, R. Lucken, T. Lafleur, A. Bourdon, and P. Chabert, “The effects of secondary electron emission on plasma sheath characteristics and electron transport in an ExB discharge via kinetic simulations,” *Plasma Sources Science and Technology*, vol. 27, p. 124001, dec 2018.
  - [22] S. Tsikata, C. Honoré, N. Lemoine, and D. M. Grésillon, “Three-dimensional structure of electron density fluctuations in the Hall thruster plasma: ExB mode,” *Physics of Plasmas*, vol. 17, no. 11, p. 112110, 2010.
  - [23] F. Taccogna and P. Minelli, “Three-dimensional particle-in-cell model of Hall thruster: The discharge channel,” *Physics of Plasmas*, vol. 25, no. 6, p. 061208, 2018.
  - [24] V. Croes, T. Lafleur, Z. Bonaventura, A. Bourdon, and P. Chabert, “2d particle-in-cell simulations of the electron drift instability and associated anomalous electron transport in Hall-effect thrusters,” *Plasma Sources Science and Technology*, vol. 26, p. 034001, feb 2017.
  - [25] S. Janhunen, A. Smolyakov, D. Sydorenko, M. Jimenez, I. Kaganovich, and Y. Raitses, “Evolution of the electron cyclotron drift instability in two-dimensions,” *Physics of Plasmas*, vol. 25, no. 8, p. 082308, 2018.
  - [26] F. Petronio, A. Tavant, T. Charoy, A. Alvarez Laguna, A. Bourdon, and P. Chabert, “Conditions of appearance and dynamics of the modified two-stream instability in  $\mathbf{E} \times \mathbf{B}$  discharges,” *Physics of Plasmas*, vol. 28, p. 043504, Apr. 2021.
  - [27] K. Hara, “An overview of discharge plasma modeling for Hall effect thrusters,” *Plasma Sources Science and Technology*, vol. 28, p. 044001, apr 2019.
  - [28] J.-P. Boeuf, “Tutorial: Physics and modeling of Hall thrusters,” *Journal of Applied Physics*, vol. 121, no. 1, p. 011101, 2017.
  - [29] A. Tavant, *Study of the plasma/wall interaction and erosion on a plasma thruster of low power*. PhD thesis, 2019. Thèse de doctorat, Physique des plasmas Université Paris-Saclay (ComUE) 2019.
  - [30] Z. Asadi, F. Taccogna, and M. Sharifian, “Numerical study of electron cyclotron drift instability: Application to Hall thruster,” *Frontiers in Physics*, vol. 7, p. 140, 2019.
  - [31] A. Smolyakov, T. Zintel, L. Couedel, D. Sydorenko, A. Umnov, E. Sorokina, and N. Marusov, “Anomalous electron transport in one-dimensional electron cyclotron drift turbulence,” *Plasma Physics Reports*, vol. 46, no. 5, pp. 496–505, 2020.
  - [32] M. M. Turner, A. Derzsi, Z. Donkó, D. Eremin, S. J. Kelly, T. Lafleur, and T. Mussenbrock, “Simulation benchmarks for low-pressure plasmas: Capacitive discharges,” *Physics of Plasmas*, vol. 20, no. 1, p. 013507, 2013.
  - [33] T. Charoy, J. P. Boeuf, A. Bourdon, J. A. Carlsson, P. Chabert, B. Cuenot, D. Eremin, L. Garrigues, K. Hara, I. D. Kaganovich, A. T. Powis, A. Smolyakov, D. Sydorenko, A. Tavant, O. Vermorel, and W. Villafana, “2d axial-azimuthal particle-in-cell benchmark for low-temperature partially magnetized plasmas,” *Plasma Sources Science and Technology*, vol. 28, p. 105010, oct 2019.
  - [34] “Landmark project (Low temperature magNetizeD plasMA benchmaRKs).” <https://www.landmark-plasma.com>, accessed on 04-01-2020.
  - [35] C. K. Birdsall, “Particle-in-cell charged-particle simulations, plus Monte Carlo collisions with neutral atoms, PIC-MCC,” *IEEE Transactions on Plasma Science*, vol. 19, no. 2, pp. 65–85, 1991.
  - [36] K. Hara and S. Tsikata, “Cross-field electron diffusion due to the coupling of drift-driven microinstabilities,” *Phys. Rev. E*, vol. 102, p. 023202, Aug 2020.
  - [37] P. Chabert, “What is the size of a floating sheath?,” *Plasma Sources Science and Technology*, vol. 23, p. 065042, Oct. 2014.
  - [38] C. N. Lashmore-Davies and T. J. Martin, “Electrostatic instabilities driven by an electric-current

- perpendicular to a magnetic-field,” *Nuclear Fusion*, vol. 13, no. 2, pp. 193–203, 1973.
- [39] M. Lampe, J. B. McBride, J. H. Orens, and R. N. Sudan, “Theory of beam cyclotron instability in plasmas,” *Physics Letters A*, vol. A 35, no. 2, p. 131, 1971.
- [40] L. Muschietti and B. Lembege, “Microturbulence in the electron cyclotron frequency range at perpendicular supercritical shocks,” *Journal of Geophysical Research-Space Physics*, vol. 118, no. 5, pp. 2267–2285, 2013.
- [41] S. Janhunen, A. Smolyakov, O. Chapurin, D. Sydorenko, I. Kaganovich, and Y. Raitses, “Nonlinear structures and anomalous transport in partially magnetized ExB plasmas,” *Physics of Plasmas*, vol. 25, no. 1, p. 011608, 2018.
- [42] P. J. Barrett, B. D. Fried, C. F. Kennel, J. M. Sellen, and R. J. Taylor, “Cross-field current-driven ion acoustic instability,” *Phys. Rev. Lett.*, vol. 28, pp. 337–340, Feb 1972.
- [43] F. F. Chen, “Excitation of drift instabilities in thermionic plasmas,” *Journal of Nuclear Energy. Part C, Plasma Physics, Accelerators, Thermonuclear Research*, vol. 7, pp. 399–417, Jan 1965.
- [44] J. Cavalier, N. Lemoine, G. Bonhomme, S. Tsikata, C. Honoré, and D. Grésillon, “Hall thruster plasma fluctuations identified as the ExB electron drift instability: Modeling and fitting on experimental data,” *Physics of Plasmas*, vol. 20, no. 8, p. 082107, 2013.
- [45] V. Jonquieres, F. Pechereau, A. Alvarez Laguna, A. Bourdon, O. Vermorel, and B. Cuenot, “A 10-moment fluid numerical solver of plasma with sheaths in a hall effect thruster,” in *2018 Joint Propulsion Conference*, p. 4905, 2018.
- [46] V. Jonquieres, *Modélisation et simulation numérique des moteurs à effet Hall*. PhD thesis, Institut National Polytechnique de Toulouse, 4 2019.
- [47] L. Y. Gicquel, N. Gourdain, J.-F. Boussuge, H. Deniau, G. Staffelbach, P. Wolf, and T. Poinso, “High performance parallel computing of flows in complex geometries,” *Comptes Rendus Mécanique*, vol. 339, no. 2, pp. 104 – 124, 2011. High Performance Computing.
- [48] T. Schonfeld and M. Rudgyard, “Steady and unsteady flow simulations using the hybrid flow solver AVBP,” *AIAA Journal*, vol. 37, no. 11, pp. 1378–1385, 1999.
- [49] N. Gourdain, L. Gicquel, M. Montagnac, O. Vermorel, M. Gazaix, G. Staffelbach, M. Garcia, J.-F. Boussuge, and T. Poinso, “High performance parallel computing of flows in complex geometries: I. methods,” *Computational Science & Discovery*, vol. 2, p. 015003, Nov 2009.
- [50] A. Haselbacher, F. Najjar, and J. Ferry, “An efficient and robust particle-localization algorithm for unstructured grids,” *Journal of Computational Physics*, vol. 225, pp. 2198–2213, 08 2007.
- [51] G. Karypis and V. Kumar, “MeTis: Unstructured Graph Partitioning and Sparse Matrix Ordering System, Version 4.0.” <http://www.cs.umn.edu/~metis>, 2009.
- [52] E. Agullo, L. Giraud, and L. Poirel, “Robust coarse spaces for abstract Schwarz preconditioners via generalized eigenproblems,” in *International conference on domain decomposition methods, DD24*, (Svalbard, Norway), Feb. 2017.
- [53] L. Poirel, *Méthodes de décomposition de domaine algébriques pour solveurs hybrides (direct-iteratif)*. PhD thesis, Ecole doctorale de mathématiques et d’informatique de l’université de Bordeaux, 11 2018.
- [54] S. Balay, S. Abhyankar, M. F. Adams, J. Brown, P. Brune, K. Buschelman, L. Dalcin, A. Dener, V. Eijkhout, W. D. Gropp, D. Karpeyev, D. Kaushik, M. G. Knepley, D. A. May, L. C. McInnes, R. T. Mills, T. Munson, K. Rupp, P. Sanan, B. F. Smith, S. Zampini, H. Zhang, and H. Zhang, “PETSc Web page.” <https://www.mcs.anl.gov/petsc>, 2019.
- [55] S. Balay, S. Abhyankar, M. F. Adams, J. Brown, P. Brune, K. Buschelman, L. Dalcin, A. Dener, V. Eijkhout, W. D. Gropp, D. Karpeyev, D. Kaushik, M. G. Knepley, D. A. May, L. C. McInnes, R. T. Mills, T. Munson, K. Rupp, P. Sanan, B. F. Smith, S. Zampini, H. Zhang, and H. Zhang, “PETSc users manual,” Tech. Rep. ANL-95/11 - Revision 3.14, Argonne National Laboratory, 2020.
- [56] R. Falgout and U. Yang, *hypre: a Library of High Performance Preconditioners*. 2002.
- [57] J. Adam, A. Serveniére, and A. Langdon, “Electron sub-cycling in particle simulation of plasma,” *Journal of Computational Physics*, vol. 47, pp. 229–244, 1982.

- [58] S. Harase, “Maximally equidistributed pseudorandom number generators via linear output transformations,” *Mathematics and Computers in Simulation*, vol. 79, pp. 1512–1519, 2009.
- [59] F. F. Panneton, P. L. Écuyer, and M. Matsumoto, “Improved long-period generators based on linear recurrences modulo 2,” *ACM Transactions on Mathematical Software*, vol. 32, pp. 1–16, 2006.
- [60] W. H. Press, S. A. Teukolsky, W. T. Vetterling, and B. P. Flannery, *Numerical Recipes 3rd Edition: The Art of Scientific Computing*. USA: Cambridge University Press, 3 ed., 2007.
- [61] I. DesJardin, K. Hara, and S. Tsikata, “Self-organized standing waves generated by ac-driven electron cyclotron drift instabilities,” *Applied Physics Letters*, vol. 115, no. 23, p. 234103, 2019.
- [62] F. Taccogna, R. Schneider, S. Longo, and M. Capitelli, “Kinetic simulations of a plasma thruster,” *Plasma Sources Science and Technology*, vol. 17, p. 024003, may 2008.
- [63] A. Domínguez-Vázquez, F. Taccogna, and E. Ahedo, “Particle modeling of radial electron dynamics in a controlled discharge of a Hall thruster,” *Plasma Sources Science and Technology*, vol. 27, p. 064006, jun 2018.
- [64] A. Domínguez-Vázquez, F. Taccogna, P. Fajardo, and E. Ahedo, “Parametric study of the radial plasma-wall interaction in a Hall thruster,” *Journal of Physics D: Applied Physics*, vol. 52, p. 474003, sep 2019.
- [65] J. C. Adams, P. N. Swarztrauber, and R. Sweet, “Fishpack90: Efficient fortran subprograms for the solution of separable elliptic partial differential equations,” *Astrophysics Source Code Library*, pp. ascl-1609, 2016.
- [66] P. Mertmann, D. Eremin, T. Mussenbrock, R. P. Brinkmann, and P. Awakowicz, “Fine-sorting one-dimensional particle-in-cell algorithm with monte-carlo collisions on a graphics processing unit,” *Computer Physics Communications*, vol. 182, no. 10, pp. 2161 – 2167, 2011.
- [67] G. Marsaglia, “Xorshift rngs,” *Journal of Statistical Software*, vol. 8, no. 14, pp. 1 – 6, 2003.
- [68] L. Garrigues, G. Fubiani, and J. Boeuf, “Appropriate use of the particle-in-cell method in low temperature plasmas: Application to the simulation of negative ion extraction,” *Journal of Applied Physics*, vol. 120, no. 21, p. 213303, 2016.
- [69] K. Bowers, “Accelerating a particle-in-cell simulation using a hybrid counting sort,” *Journal of Computational Physics*, vol. 173, no. 2, pp. 393–411, 2001.
- [70] O. Schenk and K. Gartner, “Solving unsymmetric sparse systems of linear equations with pardiso,” *Journal of Future Generation Computer Systems*, vol. 20, no. 3, pp. 475–487, 2004.
- [71] H. Okuda and C. K. Birdsall, “Collisions in a plasma of finite size particles,” *The Physics of Fluids*, vol. 13, no. 8, pp. 2123–2134, 1970.
- [72] M. M. Turner, “Kinetic properties of particle-in-cell simulations compromised by monte carlo collisions,” *Physics of Plasmas*, vol. 13, no. 3, p. 033506, 2006.